Hu *et al. Chem Synth* 2023;3:4
DOI: 10.20517/cs.2022.32

Chemical Synthesis

Research Article

Open Access

Trapezohedral platinum nanocrystals with high-index facets for high-performance hydrazine electrooxidation

Sheng-Nan Hu[1], Na Tian[1,*], Meng-Ying Li[2], Chi Xiao[1], Yao-Yin Lou[1,*], Zhi-You Zhou[1], Shi-Gang Sun[1]

[1]State Key Laboratory of Physical Chemistry of Solid Surfaces, Collaborative Innovation Center of Chemistry for Energy Materials, College of Chemistry and Chemical Engineering, Xiamen University, Xiamen 361005, Fujian, China.
[2]Hubei Collaborative Innovation Center for Advanced Organic Chemical Materials & Key Laboratory for the Synthesis and Application of Organic Functional Molecules, Hubei University, Wuhan 430062, Hubei, China.

[*]**Correspondence to:** Prof. Na Tian, State Key Laboratory of Physical Chemistry of Solid Surfaces, Collaborative Innovation Center of Chemistry for Energy Materials, College of Chemistry and Chemical Engineering, Xiamen University, 422 Siming South Road, Xiamen 361005, Fujian, China. E-mail: tnsd@xmu.edu.cn; Dr. Yao-Yin Lou, State Key Laboratory of Physical Chemistry of Solid Surfaces, Collaborative Innovation Center of Chemistry for Energy Materials, College of Chemistry and Chemical Engineering, Xiamen University, 422 Siming South Road, Xiamen 361005, Fujian, China. E-mail: louyaoyin13@mails.ucas.ac.cn

How to cite this article: Hu SN, Tian N, Li MY, Xiao C, Lou YY, Zhou ZY, Sun SG. Trapezohedral platinum nanocrystals with high-index facets for high-performance hydrazine electrooxidation. *Chem Synth* 2023;3:4. https://dx.doi.org/10.20517/cs.2022.32

Received: 22 Oct 2022 **First Decision:** 30 Nov 2022 **Revised:** 22 Dec 2022 **Accepted:** 30 Dec 2022 **Published:** 9 Jan 2023

Academic Editors: Bao-Lian Su, Yan-Xin Chen **Copy Editor:** Ke-Cui Yang **Production Editor:** Ke-Cui Yang

Abstract

Direct hydrazine fuel cell is a promising portable energy conversion device due to its high energy density and free of carbon emissions. To realize the practical applications, the design of highly efficient electrocatalysts for hydrazine oxidation reaction (HzOR) is crucial. Metal nanocrystals with high-index facets have abundant step sites with reactivity. In this study, we prepared trapezohedral Pt nanocrystals (TPH Pt NCs) enclosed by {311} high-index facets and investigated the catalytic performance for hydrazine oxidation. TPH Pt NCs possess a specific activity of 39.1 mA·cm^{-2} at 0.20 V, much higher than {111}-faceted octahedral (13.9 mA·cm^{-2}) and {100}-faceted cubic Pt NCs (9.11 mA·cm^{-2}). Meanwhile, TPH Pt NCs also show superior stability. Density functional theory (DFT) calculation indicates that Pt(311) facilitates the deprotonation of N_2H_4* to N_2H_3* (the rate-determining step) and improves the HzOR activity. This study is helpful for the design of advanced electrocatalysts for HzOR, especially high-index faceted Pt nanocatalysts.

Keywords: Hydrazine oxidation reaction, trapezohedral Pt nanocrystals, high-index facets, electrocatalysis

INTRODUCTION

Hydrazine (N_2H_4) is one of the most promising substitutes for hydrogen in fuel cells[1-3]. In comparison with other candidates (e.g., methanol, ethanol, and formic acid) applied in direct fuel cells, hydrazine is a carbon-free fuel with high energy density (5.5 $kW{\cdot}h{\cdot}L^{-1}$). Therefore, direct hydrazine fuel cells (DHFCs) have been recognized as one of the promising energy conversion devices due to their high theoretical potential of 1.56 V, remarkable power density, a wide range of operating temperature and no harmful products[4,5]. Furthermore, the substitution of sluggish oxygen evolution reaction in the water electrolysis system with hydrazine oxidation reaction (HzOR), which is thermodynamically more favorable ($N_2H_4 + 4OH^- \rightarrow N_2 + 4H_2O + 4e^-$, -0.33 V *vs.* RHE), can significantly reduce energy consumption for green hydrogen production[6,7].

Despite the great progress in the recent developments on DHFCs, the actual open circuit voltage is still significantly lower than the theoretical one, and a large amount of energy is consumed by the overpotential of the HzOR[8]. Therefore, the design of highly active electrocatalysts is crucial for the practical applications of DHFCs. Current studies of HzOR mainly focus on the design and fabrication of efficient electrocatalysts such as noble metal and intermetallic compounds[9-13], non-noble metals and their single atoms[14-17], and non-metallic materials[18]. The catalytic activity is closely related to the surface and electronic structure of the catalysts[19-25]. However, the effect of surface structure of metal nanocrystals on HzOR is rarely studied, especially that of high-index facets. Rosca and Koper[26,27] reported that the HzOR on bulk Pt single-crystal electrode is structure-sensitive, and the electrocatalytic activity increases in the order of Pt(110) > Pt(100) > Pt(111), indicating step sites are more active for HzOR. Because the high-index facets have a high density of atomic steps and ledges, which usually are active sites to control molecular adsorption and desorption, including oxygen reduction reaction[28], CO_2 reduction reaction[29], nitrogen reduction reaction[30], and small organic molecules oxidation reaction[31-33], it is anticipated that metal electrocatalysts with high-index facets will improve the HzOR performance. Previously, Liu *et al.* investigated the HzOR concave trisoctahedral Au nanocrystals (TOH Au NCs) enclosed by {551} high-index facets, which exhibit higher activity than Au sphere[8]. Pt group metals (e.g., Pt and Rh) are much more active than Au for HzOR[34]. However, to the best of our knowledge, there are no reports about HzOR on Pt NCs with high-index facets.

Herein, we carried out the HzOR on high-index faceted Pt NCs for the first time. We prepared trapezohedral Pt nanocrystals (TPH Pt NCs) enclosed with {311} high-index facets, octahedral Pt NCs with {111} facets and cubic Pt NCs with {100} facets by electrochemical method. It was found that TPH Pt NCs show much higher catalytic activity and stability of HzOR than octahedral and cubic Pt NCs. The activity of TPH Pt NCs just decreased by only 28% after 5000 s test, while 57% and 48% decline are observed on octahedral and cubic Pt NCs, respectively. Density functional theory (DFT) calculation demonstrates that the rate-determining step of HzOR on the three Pt surfaces of Pt(311), Pt(111) and Pt(100) is the first-step dehydrogenation of N_2H_4* to N_2H_3*, and Pt(311) shows the lowest energy barrier, which is beneficial for the HzOR activity.

EXPERIMENTAL

Electrochemical preparation of Pt NCs was performed in a standard three-electrode cell with a saturated calomel electrode (SCE) as reference electrode and a platinum plate as counter electrode. The working electrode was a glassy carbon rod (D = 6 mm, Takai Carbon Co., Ltd., Tokyo, Japan), which was controlled

by a 263A potentiostat (EG & G) with an electrochemical square-wave potential (SWP) program [Supplementary Table 1]. All potentials are versus the reversible hydrogen electrode (RHE) scale. Before electrodeposition, the glassy carbon was mechanically polished successively with alumina powder of the size of 1.0 and 0.3 μm. For preparation of Pt NCs, electrochemical cleaning was performed at 1.5 V for 2 s and nucleation process was conducted at 0.28 V for 0.14 s. TPH Pt NCs were prepared in the solution of 2 mM H_2PtCl_6 + 0.1 M H_2SO_4, with SWP of lower potential (E_L) at 0.42 V and upper potential (E_U) at 1.39 V for 30 min (f = 100 Hz)[35]. Cubic Pt NCs were obtained by electrochemically etching THH Pt NCs in 0.1 M H_2SO_4 with SWP of E_U at 1.5 V and E_L at 0.45 V for 15 min (f = 100 Hz)[36]. The OTH Pt NCs were electrochemically prepared in 2 mM H_2PtCl_6 + 0.1 M Na_2SO_4 with SWP of E_L at 0.38 V and E_U at 1.30 V for 8 min (f = 100 Hz). The morphology and structure of Pt NCs were characterized by scanning electron microscopy (SEM, Hitachi S-4800) and transmission electron microscopy (TEM, JEM-2100 at 200 kV).

Prior to each electrochemical measurement, the electrolyte solution was deoxygenated by bubbling high-purity N_2 for 20 min. The electrochemical measurements of HzOR were conducted in 0.5 M N_2H_4 + 1 M KOH solution and the scan rate is 10 mV s^{-1}. The electrochemical impedance spectroscopy (EIS) was recorded in a frequency range from 0.1 Hz to 1 MHz at 0.20 V.

RESULTS AND DISCUSSION

The Pt NCs are electrodeposited on a glassy carbon electrode using a programmed square-wave potential method [Supplementary Table 1]. The SEM images of TPH Pt NCs, OTH Pt NCs, and cubic Pt NCs are shown in Figure 1. The corresponding average sizes were about 139, 110 and 91 nm, respectively. The inset provided the atomic model of the corresponding facets: TPH Pt NCs are enclosed by 24 {*hkk*} ($h > k > 0$) high-index facets, OTH and cubic Pt NCs are enclosed by {111} and {100} low-index facets, respectively. The Miller indices of TPH Pt NCs were determined by measuring the plane angle in the TEM image along the [001] orientation [Supplementary Figure 1]. The average values of angles α and β were 142.0° and 128.1°, respectively, which are near to the theoretical values of 143.1° and 126.9° for {311} facets, and thus the TPH Pt NCs are denoted as TPH Pt-{311} NCs. The {311} facet is composed of a two-atomic-width (100) terrace separated by a monatomic (111) step. The 4-fold-symmetrical SAED pattern confirms that the nanoparticle is of single crystalline. From HRTEM image of TPH Pt NC [Supplementary Figure 2], the {311} step sites could be observed directly. The formation of high-index faceted Pt NCs can be ascribed to the repetitive adsorption/desorption of oxygen species on the Pt NCs induced by the SWP[35]. However, over intensive etching at high E_U of SWP can remove Pt step atoms and result in the formation of cubic or octahedral Pt NCs[36].

The surface structure of the as-prepared Pt NCs was further characterized by cyclic voltammetry (CV) in deaerated 0.1 M H_2SO_4 solution. As shown in Figure 1D, the obtained CV curves could be divided into three regions, including the H_{UPD} (underpotentially deposited hydrogen) region at the potential of 0.05 ~ 0.40 V (*vs.* RHE), the double layer region at 0.40 ~ 0.70 V, and the region of oxygen species adsorption at 0.70 ~ 1.05 V. The electrochemically active surface area (ECSA) could be determined by the charge of hydrogen adsorption/desorption (Q_H) normalized by 210 μC·cm^{-2}. The CV curves could also provide characteristic fingerprints of the Pt NCs. For example, the small shoulder at around 0.36 V on cubic Pt-{100} NCs is a characteristic peak of two-dimensional (100) surface domains or (100) terrace[31,37]. TPH Pt-{311} NCs hold the highest peak of (100) step at around 0.28 V, and the OTH Pt-{111} NCs show the highest peak of (111) step at around 0.12 V. In the region of oxygen species adsorption, the current related to the adsorption/desorption of oxygen species on the TPH Pt-{311} NCs is 0.049 mA·cm^{-2}, which is considerably larger than that on OTH Pt-{111} NCs (0.031 mA·cm^{-2}) and cubic Pt-{100} NCs (0.027 mA·cm^{-2}). This initial oxygen adsorption at low potentials is mainly attributed to oxygen atoms

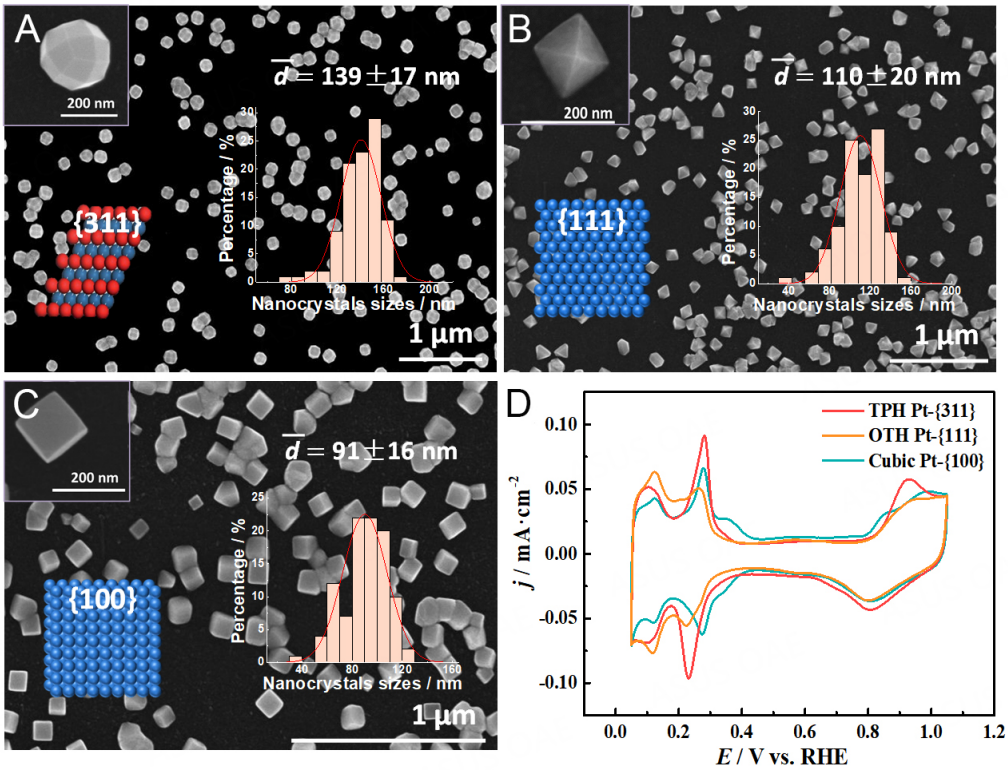

Figure 1. SEM images of (A) trapezohedral (TPH) Pt NCs; (B) octahedral (OTH) Pt NCs; and (C) cubic Pt NCs. The inset presents high magnification SEM image, size histogram and atomic model of the facet. (D) Cyclic voltammograms of the TPH, OTH, and cubic Pt NCs recorded in 0.1 M H_2SO_4 at 50 mV s^{-1}.

adsorbed on Pt step atoms with low coordination numbers[32]. This result supports that TPH Pt-{311} NCs have a high density of step atoms.

The performance of the as-prepared catalysts for HzOR was evaluated. Figure 2A shows the CV curve of HzOR on TPH Pt-{311} NCs in an Ar-saturated 0.5 M N_2H_4 + 1.0 M KOH solution at room temperature. High oxidation current can be seen on TPH Pt-{311} NCs and the current increases with the increase of potential, while the bare glassy carbon electrode is almost inert to the HzOR. The onset potential of HzOR on TPH Pt-{311} NCs is about 0.1 V, close to the value on bulk Pt(110) with step atoms, much lower than that of Pt(100) and Pt(111) reported previously[27]. The hysteresis loop in the CV curve of HzOR on TPH Pt NCs might be caused by the decrease of N_2H_4 concentration near electrode surface in the positive scan due to the intensive HzOR, and the formation of some poisoning species. Figure 2B compares the linear sweep voltammetric (LSV) curves of the as-prepared catalysts, where the current density is normalized by the geometric area. The current density on TPH Pt-{311} NCs is 41.7 mA·cm^{-2}_{geo} at 0.20 V, which is much higher than 13.4 mA·cm^{-2}_{geo} on OTH Pt-{111} NCs and 9.7 mA·cm^{-2}_{geo} on cubic Pt-{100} NCs, demonstrating that the TPH Pt-{311} NCs have a high activity for HzOR. The catalysts were further tested for oxygen evolution reaction (OER) in 1.0 M KOH solution [Figure 2B]. Obviously, the TPH Pt-{311} NCs only need 0.12 V to acquire a current density of 6.0 mA·cm^{-2}_{geo} in HzOR, which is much lower than the potential of 1.94 V in OER. This result indicates that the substitution of OER with HzOR in the water electrolysis system can significantly improve energy conversion efficiency.

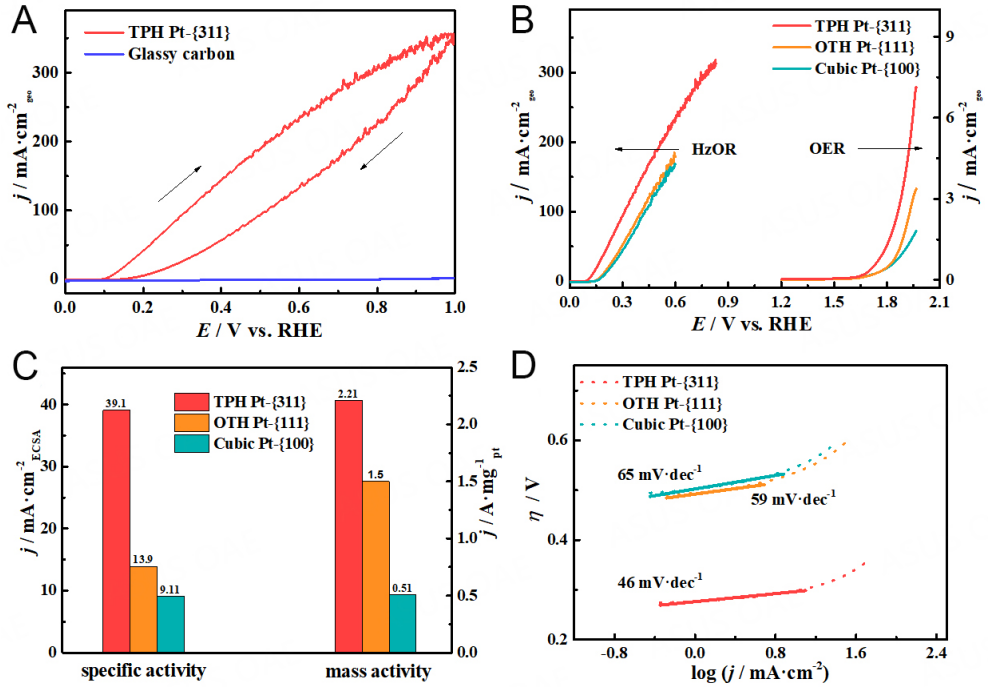

Figure 2. (A) CV curves of HzOR on TPH Pt-{311} NCs and bare glassy carbon electrode in an Ar-saturated 0.5 M N_2H_4 + 1.0 M KOH solution; (B) LSV curves of the catalysts for HzOR and OER; (C) Specific activity and mass activity of the catalysts at 0.20 V; (D) Tafel plots of the catalysts.

The currents of HzOR on different catalysts were also normalized to the ECSA and the estimated Pt loading of the catalysts [Supplementary Tables 2 and 3], as shown in Figure 2C. The specific activity and estimated mass activity of TPH Pt-{311} NCs are 39.1 mA·cm$^{-2}_{ECSA}$ and 2.21 A·mg$_{Pt}^{-1}$ at 0.20 V, respectively. The specific activity of TPH Pt-{311} NCs is 2.8-fold that of OTH Pt-{111} NCs (13.90 mA·cm$^{-2}_{ECSA}$) and 4.3-fold that of cubic Pt-{100} NCs (9.11 mA·cm$^{-2}_{ECSA}$). The high activity of TPH Pt-{311} NCs could be attributed to the high density of step sites on the surface. The Tafel slope was calculated to compare the catalytic kinetics during the HzOR [Figure 2D]. From the linear fitting of the plot of η versus log (j), the Tafel slope of TPH Pt-{311} NCs is measured to be 46 mV·dec^{-1}, which is lower than that of OTH Pt-{111} NCs (59 mV·dec^{-1}) and cubic Pt-{100} NCs (65 mV·dec^{-1}), revealing that the TPH Pt-{311} NCs have a fast charge transfer kinetic.

The stability of the catalysts for HzOR was evaluated, as shown in Figure 3A. A sudden decrease in the current density at the initial stage can be observed for all the three catalysts. The current density of the TPH Pt-{311} NCs only decreased by 28% of the initial activity after 5000 s at 0.20 V; however, the OTH Pt-{111} NCs and cubic Pt-{100} NCs decreased by 57% and 48%, respectively. After the stability test, the remained specific activity of the TPH Pt-{311} NCs is 28.2 mA·cm$^{-2}_{ECSA}$, which was 4.7-fold (5.98 mA·cm$^{-2}_{ECSA}$) that of OTH Pt-{111} NCs and 5.9-fold (4.74 mA·cm$^{-2}_{ECSA}$) that of cubic Pt-{100} NCs [Figure 3B]. The estimated mass activity of the TPH Pt-{311} NCs is 1.59 A·mg$_{Pt}^{-1}$, which is 2.4-fold (0.65 A·mg$_{Pt}^{-1}$) that of OTH Pt-{111} NCs and 5.9-fold (0.27 A·mg$_{Pt}^{-1}$) that of cubic Pt-{100} NCs. These results indicate a high catalytic stability of TPH Pt-{311} NCs. After 5000 s of the HzOR electrolysis, the shape of TPH Pt NCs is still well preserved [Supplementary Figure 3], indicating that the catalyst structure has not been damaged significantly. The 28% activity decline of TPH Pt NCs observed here may be mainly caused by the poisoning of the catalyst by the formation of the *NOx and *N, which may strongly adsorb on the catalyst surface and poison the catalyst[38,39].

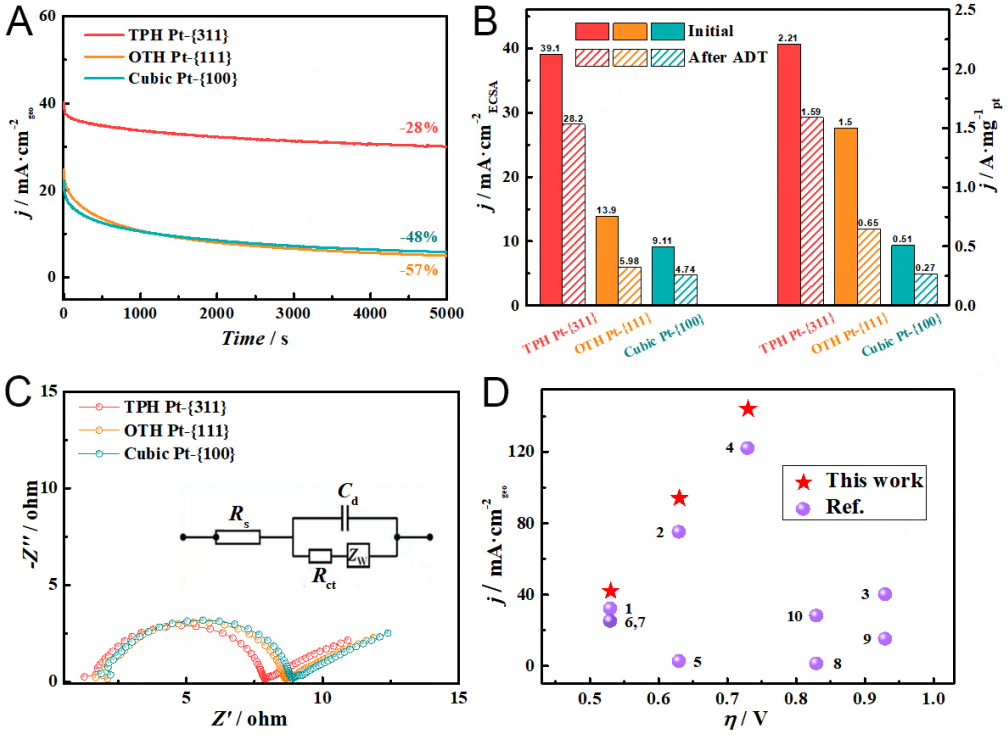

Figure 3. (A) Chronoamperometric test of the as-prepared catalysts at 0.20 V *vs.* RHE in 0.5 M N_2H_4 + 1 M KOH solution; (B) Specific activity and mass activity at 0.20 V of the as-prepared catalysts before and after accelerated durability tests (ADT) of 5000 s at 0.20 V; (C) EIS of TPH Pt-{311} NCs, OTH Pt-{111} NCs and cubic Pt-{100} NCs at 0.20 V (inset: equivalent circuit used for data analyses, R_s and R_{ct} are the ohmic and charge-transfer resistance, respectively); (D) HzOR activities of TPH Pt-{311} NCs compared with the reference results shown in Supplementary Table 4.

Figure 3C shows the electrochemical impedance spectroscopy (EIS) of the as-prepared catalysts at 0.20 V. The charge-transfer resistance (R_{ct}) reflects the kinetics of electrocatalysis on the catalysts, and a lower R_{ct} value corresponds to a faster reaction rate. TPH Pt-{311} NCs exhibit a smaller R_{ct} of 6.4 Ω than that of OTH Pt-{111} NCs (7.0 Ω) and cubic Pt-{100} NCs (7.2 Ω), indicating that a fast charge transport rate at the catalyst/electrolyte interface of TPH Pt-{311} NCs, which is consistent with the activity tendency observed in the LSV test for HzOR. Compared with the catalysts reported in recent studies[40-42], TPH Pt-{311} NCs exhibit an outstanding activity for HzOR, as shown in Figure 3D and Supplementary Table 4.

To understand the reaction mechanism and different catalytic activity of TPH Pt-{311} NCs, OTH Pt-{111} NCs and cubic Pt-{100} NCs, density functional theory (DFT) calculation of HzOR on Pt(311), Pt(111) and Pt(100) planes are conducted. The slab models of N_2H_4 adsorption on Pt(311), Pt(111) and Pt(100) are first given to reveal the charge density difference of N_2H_4* [Figure 4A]. Charge density difference analysis (CDDA) indicates prominent charge transfer from the N atoms in N_2H_4 to the nearby Pt atoms. The Bader charge analysis indicates that the electron transferred is -0.98, -1.57, and -1.82 *e* on Pt(311), Pt(111), and Pt(100), respectively. Less electron transfer suggests weaker interaction between $N_2H_4^*$ and Pt(311). The N-H bond length in N_2H_4* on Pt(311) (1.027-1.029 Å) becomes longer relative to the free molecule (1.024-1.026 Å), indicating a weaker N-H bond of N_2H_4* and thus accelerating the HzOR process.

The elementary reactions for stepwise N_2H_4 dehydrogenation ($N_2H_4 \rightarrow N_2H_4^* \rightarrow N_2H_3^* \rightarrow N_2H_2^* \rightarrow N_2H^* \rightarrow N_2^*$) are investigated on the three Pt planes. The adsorption of N_2H_4 on all the three Pt planes is thermodynamically spontaneous, which makes the catalysts easily covered by the N_2H_4* at the initial stage.

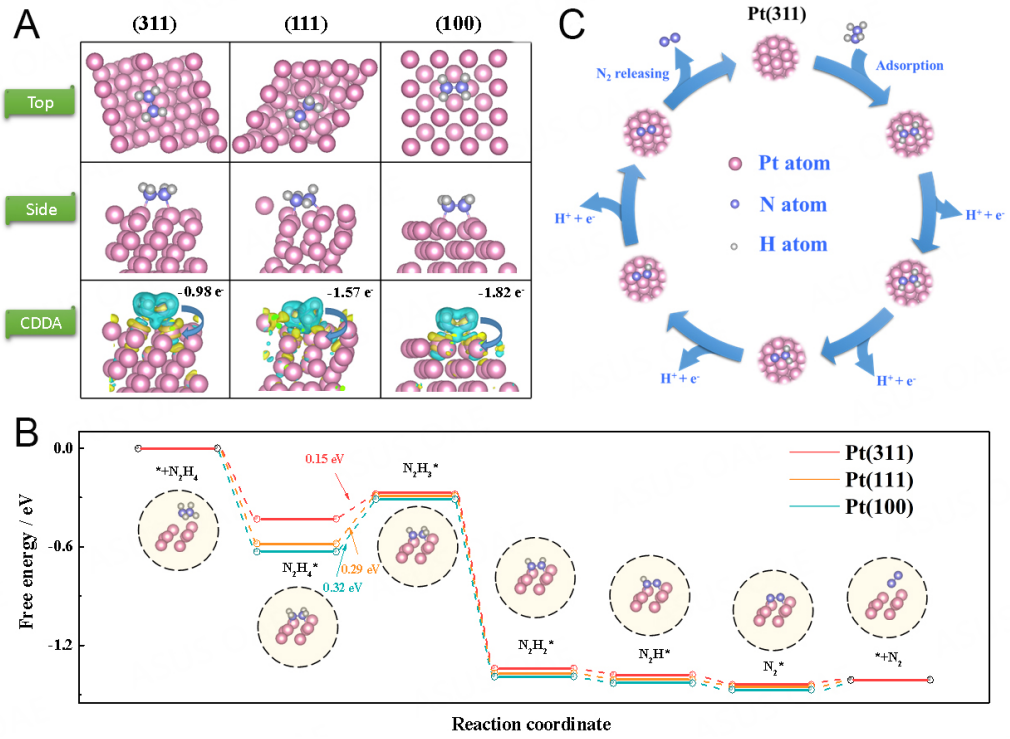

Figure 4. (A) The structural model of N_2H_4 adsorption on Pt(311), Pt(111), and Pt(100) planes, and the corresponding CDDA, where the yellow and cyan regions indicate the accumulation and depletion of the charge, respectively; (B) Free energy profiles of stepwise dehydrogenation of N_2H_4 on different Pt planes; (C) Proposed pathway of the HzOR on Pt(311). The pink, blue and grey balls represent Pt, N and H atoms, respectively.

The initial dehydrogenation of N_2H_4* to N_2H_3* is endothermic on all the studied surfaces, and is the rate-determining step (RDS) of HzOR since this step holds the highest energy barrier. For Pt(311), the energy barrier of the initial dehydrogenation of N_2H_4* to N_2H_3* is 0.15 eV, which is much lower than that on Pt(111) and Pt(100) (0.29 and 0.32 eV, respectively). The lower energy barrier of RDS on Pt(311) compared with that of Pt(111) and Pt(100) verify that Pt(311) is a highly active surface for HzOR. Note that unlike N_2H_4 oxidation on Au high-index planes where each step dehydrogenation from N_2H_4* to N_2H is endothermic[8], only the N_2H_4* to N_2H_3* on Pt is endothermic and the N_2H_4* can adsorb on Pt strongly due to high reactivity of Pt.

From the free energy profiles of N_2H_4 stepwise dehydrogenation [Figure 4B], the low RDS energy barrier of N_2H_4* to N_2H_3* mainly comes from the low adsorption energy of N_2H_4* on Pt(311). This is an unexpected phenomenon, because the low-coordinated Pt step atoms [coordination number (CN) = 7] on Pt(311) high-index plane can interact with adsorbates more strongly than flat Pt(111) and Pt(100) (CN = 9 and 8, respectively), yielding a higher adsorption energy. We then analyzed the Pt-N bond length and adsorption configuration. The Pt-N bond length of N_2H_4* on Pt(311) is 2.153-2.155 Å, which is longer than that of Pt(111) (2.146-2.148 Å) and Pt(100) (2.132-2.134 Å). Longer Pt-N bond length indicates weaker adsorption of N_2H_4* on Pt(311), which is favorable for the reduction of the energy barrier from N_2H_4* to N_2H_3*, because the binding of N_2H_4* is too strong according to the free energy profile curve [Figure 4B]. We analyzed the adsorption structure of N_2H_4* on Pt(311). It is *via* two N atoms preferentially coordinating with two low-coordinated Pt atoms on the surface. Because the *s* and *p* orbitals of N atoms are relatively discrete and the rich step sites on high-index plane will result in large space steric effect, the adsorption of N_2H_4* on Pt(311) will elongate the adjacent Pt-Pt distance (increasing from 2.774-2.776 to 2.793-2.795 Å after the

Table 1. Calculated Gibbs free energies of elementary steps for electrocatalytic hydrazine oxidation reaction on Pt(311), Pt(111) and Pt(100), respectively

Elementary steps	Gibbs free energies (ΔG)/eV		
	Pt(311)	Pt(111)	Pt(100)
$N_2H_4 + * \rightarrow N_2H_4*$	-0.43	-0.58	-0.63
$N_2H_4* \rightarrow N_2H_3* + H^+ + e^-$	0.15	0.29	0.32
$N_2H_3* \rightarrow N_2H_2* + H^+ + e^-$	-1.06	-1.08	-1.08
$N_2H_2* \rightarrow N_2H* + H^+ + e^-$	-0.04	-0.04	-0.04
$N_2H* \rightarrow N_2* + H^+ + e^-$	-0.04	-0.04	-0.04
$N_2* \rightarrow N_2 + *$	0.03	0.04	0.05
$N_2H_4* \rightarrow 2NH_2*$	0.26	0.47	0.74
$N_2H_3* \rightarrow NH* + NH_2*$	0.67	0.73	0.85
$N_2H_2* \rightarrow 2NH*$	0.34	0.52	0.59

adsorption), which will increase the system energy. In contrast, the Pt-Pt distance just changes slightly on Pt(111) (increasing from 2.774-2.776 to 2.780-2.782 Å) and Pt(100) (increasing from 2.774-2.776 to 2.776-2.778 Å). This viewpoint provides a reasonable interpretation of the unexpected low adsorption energy of $N_2H_4^*$ on high-index Pt(311) plane. Most reports about DFT calculations of HzOR mechanism only consider the change of free energy and the ΔG of transient state[43-46]. Accompanied by the four-electron transfer in the oxidation reaction of hydrazine ($N_2H_4 + 4OH^- \rightarrow N_2 + 4H_2O + 4e^-$), the free energy of adsorbed intermediates is also calculated. As shown in Table 1, the calculated Gibbs free energies of elementary steps for electrocatalytic HzOR on Pt(311), Pt(111) and Pt(100) surfaces are listed and the optimized intermediates are concomitantly displayed in Figure 4B. In our work, the analysis of Pt-N bond length and adsorption configuration provides new insight into the HzOR mechanism on Pt high-index planes.

The dehydrogenation process of HzOR on Pt is given [Figure 4C and Supplementary Figures 4 and 5]. The mechanism of HzOR on Pt(311) can be described as follows. First, as N_2H_4 is close to the surface of Pt(311), it is easily adsorbed on the step sites forming N_2H_4*. Then, N_2H_4* stepwise-dehydrogenated and finally converted to N_2, and the N-H bond cleavage and the retention of N-N bonds are facilitated by the chemisorption of N_2H_4 through both nitrogen atoms[47].

CONCLUSIONS

In summary, we synthesized TPH Pt NCs with {311} high-index facets, OTH Pt-{111} NCs, and cubic Pt-{100} NCs by electrochemical square-wave potential method. The structure-reactivity relationship of electro-oxidation of hydrazine was investigated. At 0.20 V *vs.* RHE, the specific activity is 2.8 and 4.3 times that of OTH Pt-{111} NCs and cubic Pt-{100} NCs, respectively. The catalytic activity of TPH Pt-{311} catalyst decreased by only 28% after 5000 s, while 57% and 48% are dropped on OTH Pt-{111} NCs and cubic Pt-{100} NCs, respectively. These results show that TPH Pt-{311} NCs with abundant step sites are more beneficial to HzOR than OTH Pt-{111} NCs and cubic Pt-{100} NCs. DFT calculation demonstrates that on the three Pt planes, the rate-determining step of HzOR is the first-step deprotonation from N_2H_4* to N_2H_3*, and Pt(311) has the lowest energy barrier for this step, which is beneficial to the HzOR activity. The low energy barrier mainly comes from the unexpected weak adsorption of N_2H_4* on stepped Pt(311), since the adsorption can induce the elongation of the adjacent Pt-Pt distance. This study is of importance for the design of hydrazine oxidation electrocatalysts.

DECLARATIONS

Authors' contributions

Conceived the idea of the project: Tian N, Hu SN, Lou YY

Made substantial contributions to conception and design of the study, performed data analysis and interpretation and wrote the draft of manuscript: Tian N, Zhou ZY, Hu SN, Lou YY, Li MY, Xiao C

Performed data acquisition and provided administrative, technical, and material support: Sun SG, Tian N, Zhou ZY

Discussed and revised the manuscript: Tian N, Zhou ZY, Hu SN, Lou YY

Finalized the manuscript: Sun SG, Tian N, Zhou ZY

Availability of data and materials

Not applicable.

Financial support and sponsorship

This research was financially supported by grants from National Natural Science Foundation of China (22172135, 22002131) and China Postdoctoral Science Foundation (2020M671963).

Conflicts of interest

All authors declared that there are no conflicts of interest.

Ethical approval and consent to participate

Not applicable.

Consent for publication

Not applicable.

REFERENCES

1. An L, Zhao T, Li Y. Carbon-neutral sustainable energy technology: direct ethanol fuel cells. *Renew Sust Energ Rev* 2015;50:1462-8. DOI
2. Rostamikia G, Janik MJ. Direct borohydride oxidation: mechanism determination and design of alloy catalysts guided by density functional theory. *Energy Environ Sci* 2010;3:1262. DOI
3. Ji X, Lee KT, Holden R, et al. Nanocrystalline intermetallics on mesoporous carbon for direct formic acid fuel cell anodes. *Nat Chem* 2010;2:286-93. DOI PubMed
4. Serov A, Padilla M, Roy AJ, et al. Anode catalysts for direct hydrazine fuel cells: from laboratory test to an electric vehicle. *Angew Chem* 2014;126:10504-7. DOI PubMed
5. Varcoe JR, Atanassov P, Dekel DR, et al. Anion-exchange membranes in electrochemical energy systems. *Energy Environ Sci* 2014;7:3135-91. DOI
6. Wang T, Wang Q, Wang Y, et al. Atomically dispersed semimetallic selenium on porous carbon membrane as an electrode for hydrazine fuel cells. *Angew Chem* 2019;131:13600-5. DOI PubMed
7. Xue Q, Huang H, Zhu J, et al. Au@Rh core-shell nanowires for hydrazine electrooxidation. *Appl Catal B Environ* 2020;278:119269. DOI
8. Liu F, Jiang X, Wang H, et al. Boosting electrocatalytic hydrazine oxidation reaction on high-index faceted Au concave trioctahedral nanocrystals. *ACS Sustain Chem Eng* 2022;10:696-702. DOI
9. Rees NV, Compton RG. Carbon-free energy: a review of ammonia- and hydrazine-based electrochemical fuel cells. *Energy Environ Sci* 2011;4:1255. DOI
10. Li F, Ji Y, Wang S, Li S, Chen Y. Ethylenediaminetetraacetic acid mediated synthesis of palladium nanowire networks and their enhanced electrocatalytic performance for the hydrazine oxidation reaction. *Electrochim Acta* 2015;176:125-9. DOI
11. Ensafi AA, Abarghoui MM, Rezaei B. Facile synthesis of Pt-Cu@silicon nanostructure as a new electrocatalyst supported matrix, electrochemical detection of hydrazine and hydrogen peroxide. *Electrochim Acta* 2016;190:199-207. DOI

12. Liu Y, Chen S, Wang A, Feng J, Wu X, Weng X. An ultra-sensitive electrochemical sensor for hydrazine based on AuPd nanorod alloy nanochains. *Electrochim Acta* 2016;195:68-76. DOI
13. Chen L, Jiang L, Wang A, Chen Q, Feng J. Simple synthesis of bimetallic AuPd dendritic alloyed nanocrystals with enhanced electrocatalytic performance for hydrazine oxidation reaction. *Electrochim Acta* 2016;190:872-8. DOI
14. Sakamoto T, Matsumura D, Asazawa K, et al. Operando XAFS study of carbon supported Ni, NiZn, and Co catalysts for hydrazine electrooxidation for use in anion exchange membrane fuel cells. *Electrochim Acta* 2015;163:116-22. DOI
15. Zhang C, Yuan W, Wang Q, Peng X, Liu X, Luo J. Single Cu atoms as catalysts for efficient hydrazine oxidation reaction. *ChemNanoMat* 2020;6:1474-8. DOI
16. Feng Z, Li D, Wang L, et al. In situ grown nanosheet Ni Zn alloy on Ni foam for high performance hydrazine electrooxidation. *Electrochim Acta* 2019;304:275-81. DOI
17. Tang P, Lin X, Yin H, et al. Hierarchically nanostructured nickel-cobalt alloy supported on nickel foam as a highly efficient electrocatalyst for hydrazine oxidation. *ACS Sustain Chem Eng* 2020;8:16583-90. DOI
18. Zhang T, Asefa T. Heteroatom-doped carbon materials for hydrazine oxidation. *Adv Mater* 2019;31:e1804394. DOI PubMed
19. Sápi A, Rajkumar T, Kiss J, Kukovecz Á, Kónya Z, Somorjai GA. Metallic nanoparticles in heterogeneous catalysis. *Catal Lett* 2021;151:2153-75. DOI PubMed PMC
20. Theerthagiri J, Karuppasamy K, Lee SJ, et al. Fundamentals and comprehensive insights on pulsed laser synthesis of advanced materials for diverse photo- and electrocatalytic applications. *Light Sci Appl* 2022;11:250. DOI PubMed PMC
21. Yu Y, Theerthagiri J, Lee SJ, Muthusamy G, Ashokkumar M, Choi MY. Integrated technique of pulsed laser irradiation and sonochemical processes for the production of highly surface-active NiPd spheres. *Chem Eng J* 2021;411:128486. DOI
22. Theerthagiri J, Lee SJ, Murthy AP, Madhavan J, Choi MY. Fundamental aspects and recent advances in transition metal nitrides as electrocatalysts for hydrogen evolution reaction: a review. *Curr Opin Solid State Mater Sci* 2020;24:100805. DOI
23. Xiao C, Lu B, Xue P, et al. High-index-facet- and high-surface-energy nanocrystals of metals and metal oxides as highly efficient catalysts. *Joule* 2020;4:2562-98. DOI
24. Koper MT. Structure sensitivity and nanoscale effects in electrocatalysis. *Nanoscale* 2011;3:2054-73. DOI PubMed
25. Bentley CL, Kang M, Unwin PR. Nanoscale surface structure-activity in electrochemistry and electrocatalysis. *J Am Chem Soc* 2019;141:2179-93. DOI PubMed
26. Yu N, Tian N, Zhou Z, et al. Pd nanocrystals with continuously tunable high-index facets as a model nanocatalyst. *ACS Catal* 2019;9:3144-52. DOI
27. Rosca V, Koper MT. Electrocatalytic oxidation of hydrazine on platinum electrodes in alkaline solutions. *Electrochim Acta* 2008;53:5199-205. DOI
28. Kim C, Dionigi F, Beermann V, Wang X, Möller T, Strasser P. Alloy nanocatalysts for the electrochemical oxygen reduction (ORR) and the direct electrochemical carbon dioxide reduction reaction (CO_2 RR). *Adv Mater* 2019;31:e1805617. DOI PubMed
29. Zhong H, Liu K, Zhang Q, Meng F, Bao D, Zhang X. Copper tetrazolate based metal-organic frameworks as highly efficient catalysts for artificially chemical and electrochemical CO_2 conversion. *Nano Select* 2020;1:311-9. DOI
30. Wang F, Mao L, Xie H, Mao J. Graphene derivatives and graphene composite electrocatalysts for N_2 reduction reaction. *Small Struct* 2021;2:2000075. DOI
31. Zhou Z, Shang S, Tian N, et al. Shape transformation from Pt nanocubes to tetrahexahedra with size near 10 nm. *Electrochem Commun* 2012;22:61-4. DOI
32. Tian N, Zhou ZY, Sun SG, Ding Y, Wang ZL. Synthesis of tetrahexahedral platinum nanocrystals with high-index facets and high electro-oxidation activity. *Science* 2007;316:732-5. DOI PubMed
33. Zhou ZY, Tian N, Li JT, Broadwell I, Sun SG. Nanomaterials of high surface energy with exceptional properties in catalysis and energy storage. *Chem Soc Rev* 2011;40:4167-85. DOI PubMed
34. Álvarez-ruiz B, Gómez R, Orts JM, Feliu JM. Role of the metal and surface structure in the electro-oxidation of hydrazine in acidic media. *J Electrochem Soc* 2002;149:D35. DOI
35. Xiao J, Liu S, Tian N, et al. Synthesis of convex hexoctahedral Pt micro/nanocrystals with high-index facets and electrochemistry-mediated shape evolution. *J Am Chem Soc* 2013;135:18754-7. DOI PubMed
36. Xiao C, Tian N, Li W, et al. Shape transformations of Pt nanocrystals enclosed with high-index facets and low-index facets. *CrystEngComm* 2021;23:6655-60. DOI
37. Chen Q, Vidal-iglesias FJ, Solla-gullón J, Sun S, Feliu JM. Role of surface defect sites: from Pt model surfaces to shape-controlled nanoparticles. *Chem Sci* 2012;3:136-47. DOI
38. Zhong C, Hu WB, Cheng YF. Recent advances in electrocatalysts for electro-oxidation of ammonia. *J Mater Chem A* 2013;1:3216-38. DOI
39. Chang F, Gao W, Guo J, Chen P. Emerging materials and methods toward ammonia-based energy storage and conversion. *Adv Mater* 2021;33:e2005721. DOI PubMed
40. Li J, Zhang C, Zhang C, et al. Electronic configuration of single ruthenium atom immobilized in urchin-like tungsten trioxide towards hydrazine oxidation-assisted hydrogen evolution under wide pH media. *Chem Eng J* 2022;430:132953. DOI
41. Chen S, Wang C, Liu S, et al. Boosting hydrazine oxidation reaction on CoP/Co mott-schottky electrocatalyst through engineering active sites. *J Phys Chem Lett* 2021;12:4849-56. DOI PubMed
42. Dhiman N, Pradhan D, Mohanty P. Heteroatom (N and P) enriched nanoporous carbon as an efficient electrocatalyst for hydrazine

oxidation reaction. *Fuel* 2022;314:122722. DOI

43. Yan Y, Zhang JY, Shi XR, et al. A zeolitic-imidazole framework-derived trifunctional electrocatalyst for hydrazine fuel cells. *ACS Nano* 2021;15:10286-95. DOI PubMed
44. Zhu Y, Zhang J, Qian Q, et al. Dual nanoislands on Ni/C hybrid nanosheet activate superior hydrazine oxidation-assisted high-efficiency H_2 production. *Angew Chem Int Ed Engl* 2022;61:e202113082. DOI PubMed
45. Li J, Li Y, Wang J, et al. Elucidating the critical role of ruthenium single atom sites in water dissociation and dehydrogenation behaviors for robust hydrazine oxidation-boosted alkaline hydrogen evolution. *Adv Funct Mater* 2022;32:2109439. DOI
46. Li Y, Zhang J, Liu Y, et al. Partially exposed RuP_2 surface in hybrid structure endows its bifunctionality for hydrazine oxidation and hydrogen evolution catalysis. *Sci Adv* 2020:6. DOI PubMed PMC
47. Alberas DJ, Kiss J, Liu Z, White J. Surface chemistry of hydrazine on Pt(111). *Surf Sci* 1992;278:51-61. DOI